Corrosion Behavior of Steels in Supercritical CO_2 for Power Cycle Applications

R. Repukaiti[a b], L. Teeter[a b], M. Ziomek-Moroz[a], Ö.N. Doğan[a], and J. D. Tucker[b]

[a] National Energy Technology Laboratory, U.S. Department of Energy, Albany, OR 97321, USA
[b] Oregon State University, Corvallis, OR 97331, USA

In order to understand issues with corrosion of heat exchanger materials in direct supercritical carbon dioxide (sCO_2) power cycles, a series of autoclave exposure experiments and electrochemical experiments have been conducted. Corrosion behaviors of 347H stainless steel and P91 martensitic-ferrtic steel in sCO_2 environment have been compared. In autoclave exposure tests performed at 50°C-245°C and 80 bar. Mass change measurements, surface characterization, and corrosion product analysis have been conducted to understand the corrosion behavior of steels in sCO_2 containing H_2O and O_2. Electrochemical tests performed at room temperature and 50°C, a simulation environment of water condensation phase with dissolved CO_2 was prepared to evaluate the corrosion resistance of materials. From both types of experiments, generally 347H showed higher corrosion resistance than P91.

I. Introduction

Supercritical CO_2 has been investigated for use in power cycles. These sCO_2 cycles are projected to have higher efficiencies compared to steam cycles due to reasons such as lack of phase change in working fluid within the working envelope, recompression of sCO_2 near liquid densities, and high heat recuperation. In addition to the higher efficiencies, dry or reduced water cooling in direct and indirect cycles and producing storage ready CO_2 in direct cycles will also lower the environmental impact. Furthermore, compact turbo machinery and simple configurations of the CO_2 cycles could result in lower capital cost.

Direct sCO_2 cycle is a process that utilizes pressurized combustion exhaust as working fluid and expands it through a turbine to generate power. The combustion exhaust contains primarily CO_2 in supercritical state with water and O_2 dissolved in it. Depending on the fuel (natural gas, coal derived syngas, etc.), the working fluid may contain other impurities such as SO_2 and HCl (1). The expanded working fluid goes through heat exchangers to transfer the heat to the incoming high-pressure CO_2 used for dilution in the combustor. Some of the CO_2 is diverted for sequestration after water separation.

Heat exchanger is a key part in direct sCO_2 power cycle. Corrosion resistance of heat exchanger materials is significant for its sustainability. This research is conducted to study the corrosion mechanisms of two alloys, austenitic stainless steel 347H, and martensitic-ferritic steel P91 in sCO_2 containing O_2 and H_2O impurities. The results presented are divided into two parts: autoclave exposure experiments and electrochemical experiments.

For the autoclave exposure experiments, the purpose is to evaluate the candidate materials in a simulated heat exchanger environment. The sCO_2 fluid phase contained O_2 and H_2O. The electrochemical experiments were carried out to reveal the corrosion mechanisms and measure the corrosion rates for cases where water saturated with CO_2 condenses on material surface.

II. Experimental Procedures

1. Autoclave Exposure Experiments

Alloy coupons of 347H austenitic stainless steel and P91 martensitic-ferrtic steel were machined with a size of 25 x 20 x 6 mm. Chemical compositions of the alloys are shown in Table I. Microstructures for 347H and P91 are shown in Figures 1a and 1b, respectively, and both show grain boundaries with even grain sizes. All coupons have a 1200 grit SiC paper final surface finish, and have been cleaned prior to experiments. They are exposed to a gaseous phase with a mixture of CO_2:O_2=95:1, which is combined with H_2O in three different conditions as shown in Table II. Each condition has eight samples that were hung on Teflon sleeves in a 1100 ml autoclave.

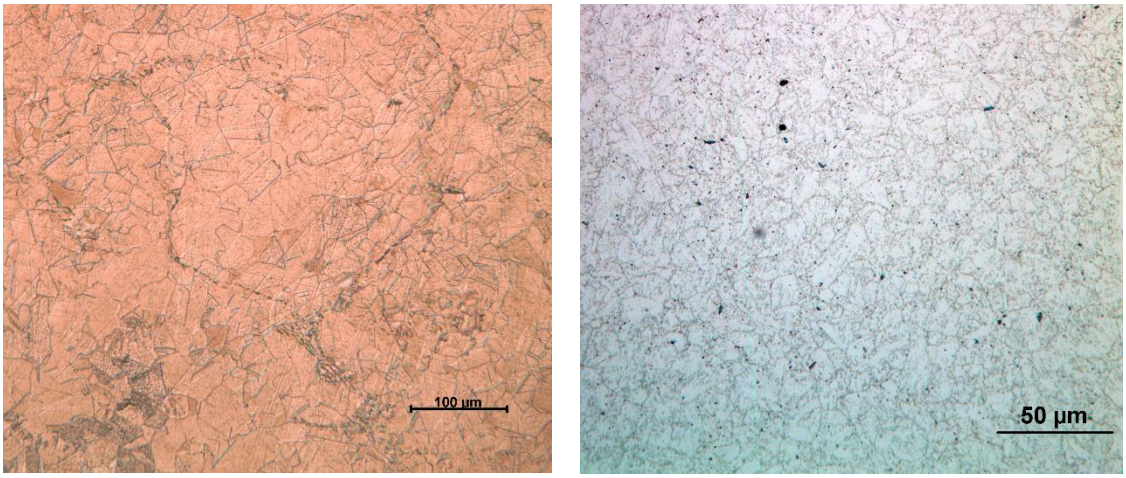

(a) 347H (b) P91

Figure 1. Microstructures of candidate alloys (2).

TABLE I. Chemical composition of alloys

Alloy	Description	Cr	Ni	C	Mn	P	S	Si	Co	Cu	Mo	N	Cb	Ti	Al	Sn	Ta	Fe
347H	Austenitic stainless steel	17.3	9.09	0.05	1.5	0.03	0.01	0.38	0.16	0.43	0.41	0.04	0.62	0.01	0.01	0.01	0.01	Balance
P91	Martensitic-ferritic steel	8.37	0.09	0.9	0.45	0.01	0.01	0.33		0.09	0.9	0.45	0.07	0.01	0.01			Balance

TABLE II. Exposure conditions

Exposure condition	Temperature (°C)	Pressure (bar)	Water Volume (ml)	Time (hours)	Shut down procedure
Condition 1	50	80	400	500	Temperature and pressure drop simultaneously
Condition 2	245	80	6.7	500	Temperature and pressure drop simultaneously
Condition 3	245	80	6.7	500	Temperature drops, then pressure drops

Exposure conditions are schematically shown in Figure 2. In condition 1, four samples were submerged in water rich phase, while the other four were exposed to sCO_2-rich phase. Conditions 1 and 2 have the same mole fraction of H_2O in CO_2 in sCO_2 rich phases, which was calculated from H_2O saturated in CO_2 at two different temperatures (3).

Conditions 2 and 3 have an identical environment prior to the end of exposure. The difference between them is H_2O condensation during the shutdown period. Figure 3 shows the temperature-pressure profiles. In condition 2, pressure and temperature were gradually lowered simultaneously. In condition 3, pressure was lowered to ambient pressure while the temperature was maintained at 245°C. After the pressure reached ambient pressure, the temperature was lowered to room temperature. As a result, condition 2 has an H_2O condensation period during shutdown, while condition 3 does not.

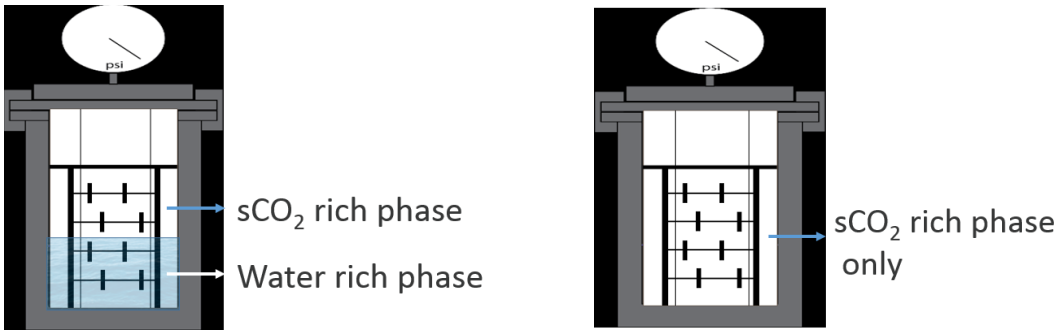

(a) Condition 1 (b) Condition 2 and 3

Figure 2. Autoclave experiments setup (4).

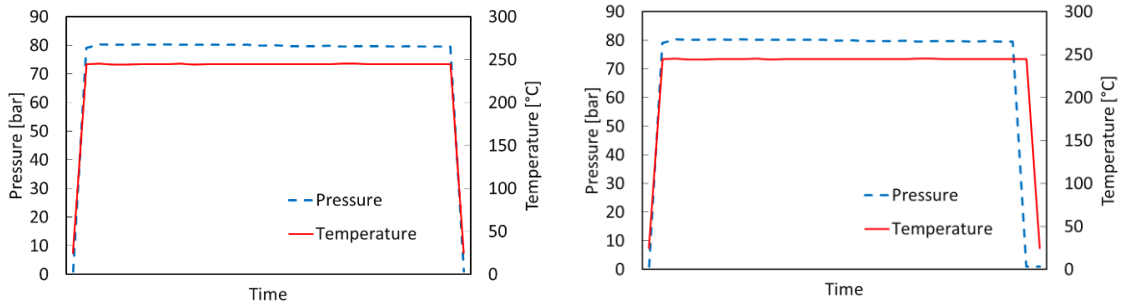

(a) Condition 2, with H2O condensation transient

(b) Condition 3, without H2O condensation transient

Figure 3. Temperature-pressure profile of condition 2 and 3.

2. Electrochemical experiments

Electrochemical tests were conducted at two different temperatures, 25 and 50°C. Electrolyte was prepared by constantly bubbling CO_2 into deionized water in order to create carbonic acid (5). The pH was measured to ensure a stable solution. As shown in Figure 4, pH is 4.1 at 25°C after bubbling CO_2 for 30 minutes, and pH is 4.2 at 50°C after same amount of time. The Counter electrode was Platinum, and the reference electrode was

saturated calomel electrode. The same alloy coupons were used as in the autoclave exposure experiments with a 1200 grit SiC paper surface finish. Types of electrochemical experiments performed are as follows:

- Linear polarization resistance, scan rate 0.125 mV/s
- Potentiodynamic scan, scan rate 5 mV/s
- Cyclic voltammetry, scan rate 5 mV/s
- Potentiostatic scan, 300 s

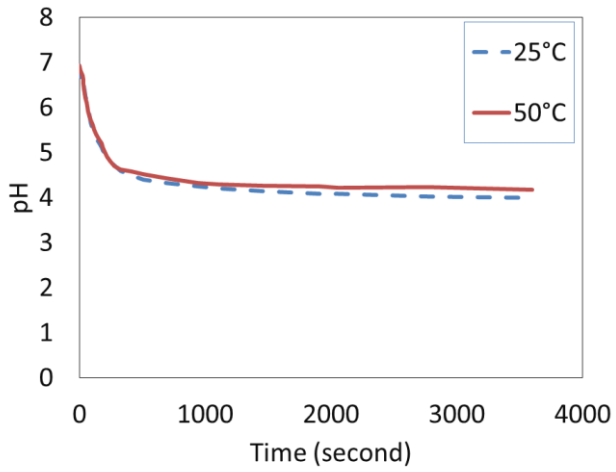

Figure 4. pH measurement of electrolyte at 25 and 50°C

III. Results and Discussion

1. Autoclave Exposure Experiments Results

Multiple findings can be concluded from the mass change results in Figures 5 and 6.

- Figures 5 and 6 show that 347H has less mass change than P91 in all conditions, which demonstrates that 347H is more corrosion resistant than P91 in the exposure environments.
- As showed in Figure 5, the coupons in H_2O rich phase experienced a negative mass change due to the dissolution of corrosion products into aqueous phase. P91 has a large error bar in CO_2 rich phase, because the coupons close to the water surface have corrosion product dissolved into water due to water splash during startup period, while the ones farther from the water surface have less influence from water splash. Because of this error, the comparison of corrosion resistance between CO_2 and H_2O rich phases needs to be determined by mass loss and corrosion rate calculation.

- As can be seen in Figure 6, the coupons in condition 3 showed less mass change than the ones in condition 2, which demonstrates that H_2O condensation is the main cause of corrosion.

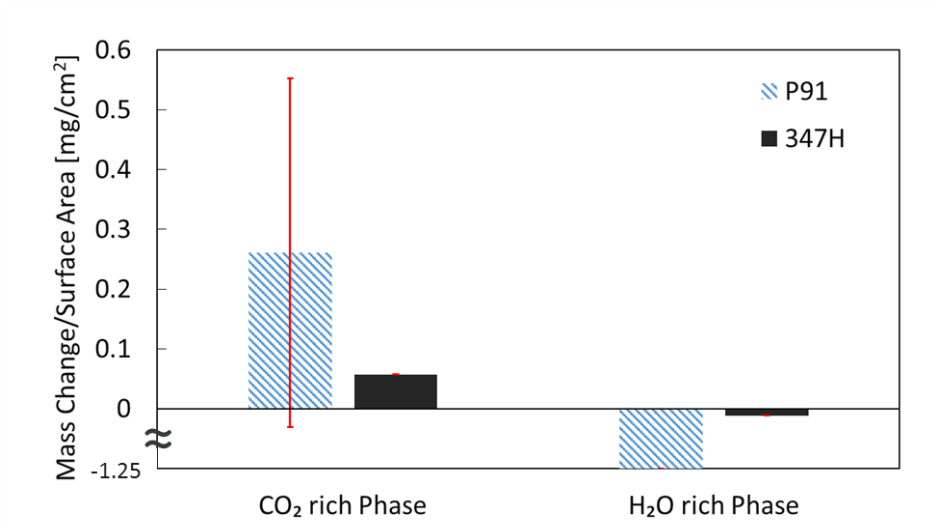

Figure 5. Mass change comparison as a function of phases at 50°C and 80 bar in condition 1.

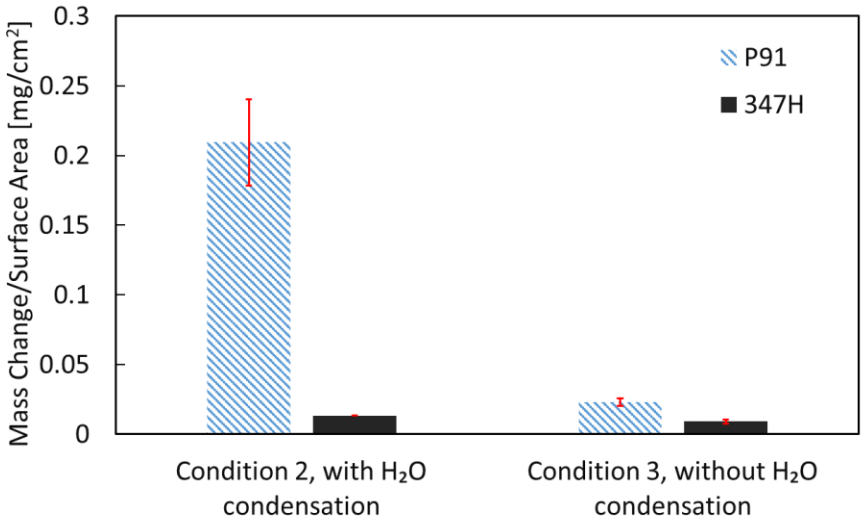

Figure 6. Mass change comparison of condition 2 and 3, as a function of Water condensation at 245°C and 80 bar in CO_2 rich phase

Sample surfaces were characterized by X-ray diffraction for coupons in conditions 1 and 2. The corrosion product layer formed on the 347H sample surface was too thin to be detected. Also, 347H has less than 0.05 mg/cm^2 mass change over all. Table III shows that on the P91 iron hydroxide products formed. but no iron carbonates. This phenomenon shows the dominant species affecting corrosion mechanisms are oxygen and water. Figure 7 shows P91's images after autoclave exposure. In conditions 1 and 2, coupons have obvious corrosion products on surfaces, while condition 3 coupons have relatively clean surfaces, which is verified by mass change results that condition 3 samples have the least mass change.

TABLE III. Glancing angle XRD results of corrosion products

Alloys	Condition 1		Condition 2	Condition 3
	sCO_2 rich phase	H_2O rich phase	sCO_2 rich phase	sCO_2 rich phase
347H	Base metal	Base metal	Base metal	TBD
P91	Hematite(Fe_2O_3) Base Metal	Hematite(Fe_2O_3) Magnetite(Fe_3O_4) Goethite(FeO(OH))	Goethite(FeO(OH)) Base Metal	TBD

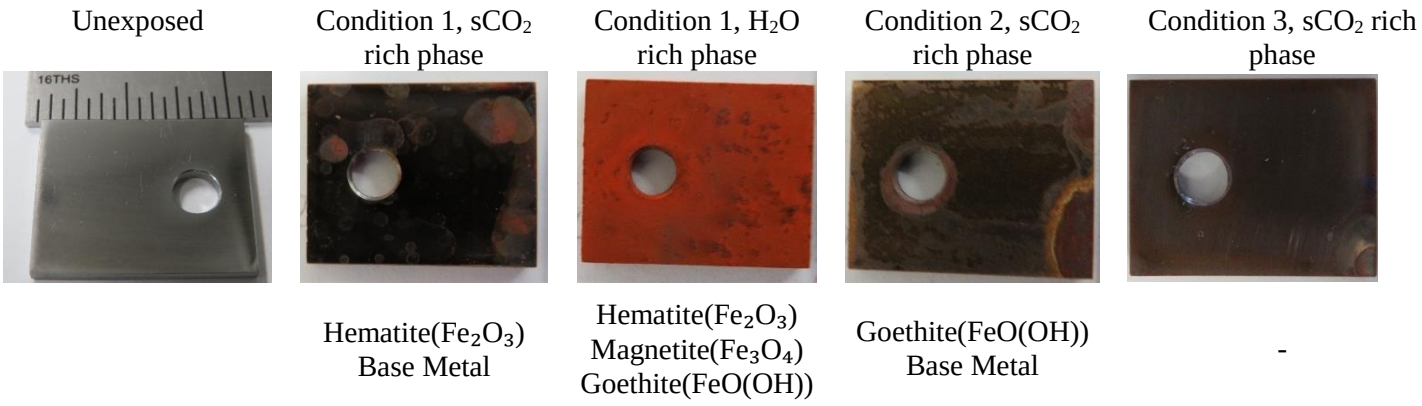

Figure 7. P91 coupon images after autoclave exposure experiments

2. Electrochemical experiments results

Results of the electrochemical experiments are shown in Figures 8 through 12. From potentiodyanmic polarization scans, alloys' anodic and cathodic parts have similar characteristics. The plots in Figure 8 both display the following regions: cathodic, active, active-passive, passive, and transpassive. Also, they both have higher corrosion current density at higher temperature extrapolated from Tafel slopes. Linear polarization resistance scans verified the same conclusion that alloys have higher corrosion current density at 50°C. Cyclic voltammetry demonstrates that P91 is prone to localized corrosion as pitting corrosion indicated from the curves at both temperatures. Potentiostatic polarization scans were conducted at primary passivation potentials selected from the potentiodynamic polarization curves for both alloys at each temperature. Potentiostatic scans prove that 347H starts passivation ahead of P91.

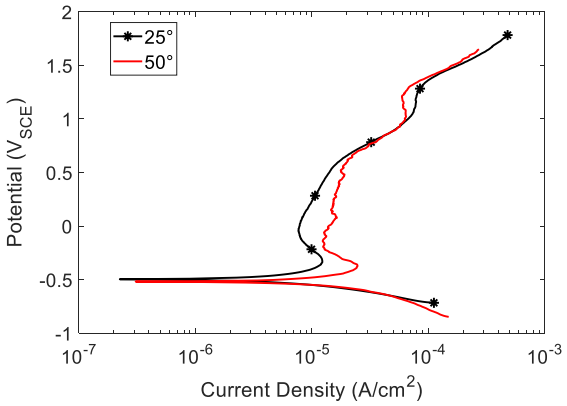

(a) 347H

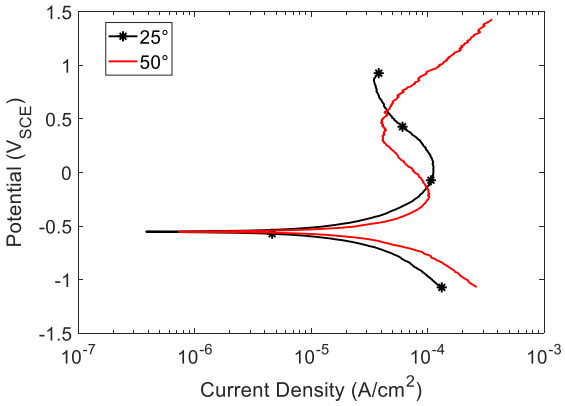

(b) P91

Figure 8. Potentiodynamic polarization scans.

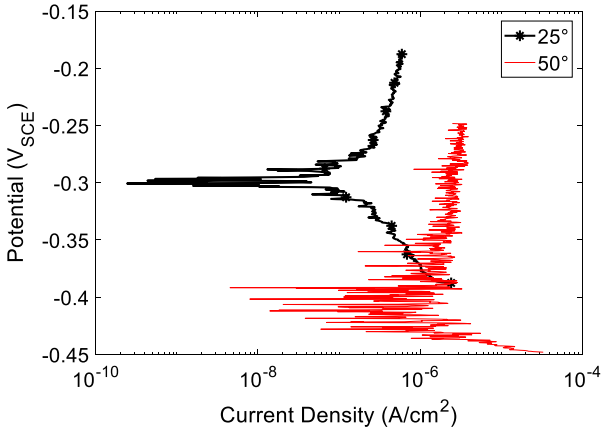

(a) Logarithmic scale

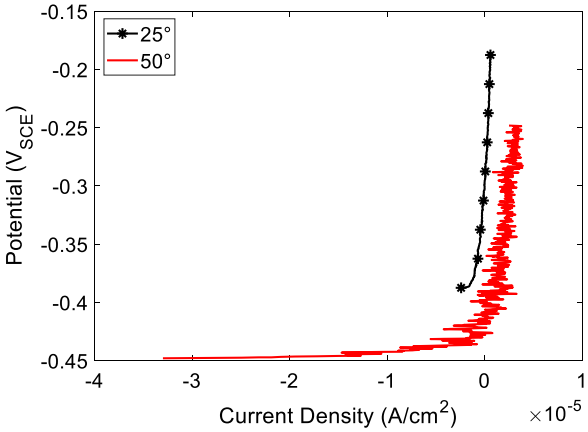

(b) Linear scale

Figure 9. 347H linear polarization resistance

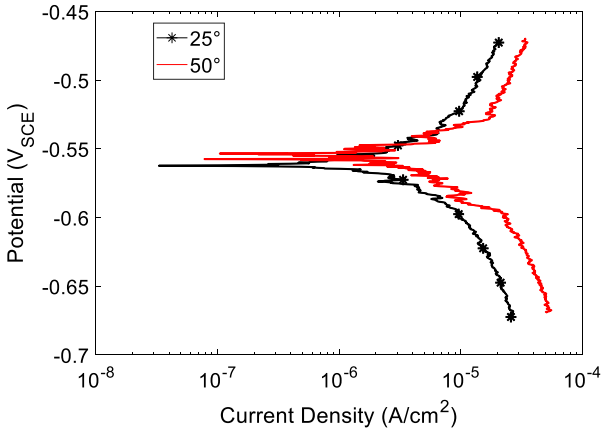

(a) Logarithmic scale

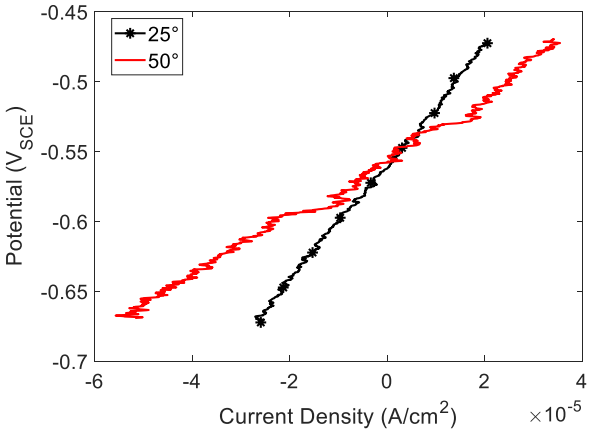

(b) Linear scale

Figure 10. P91 linear polarization resistance

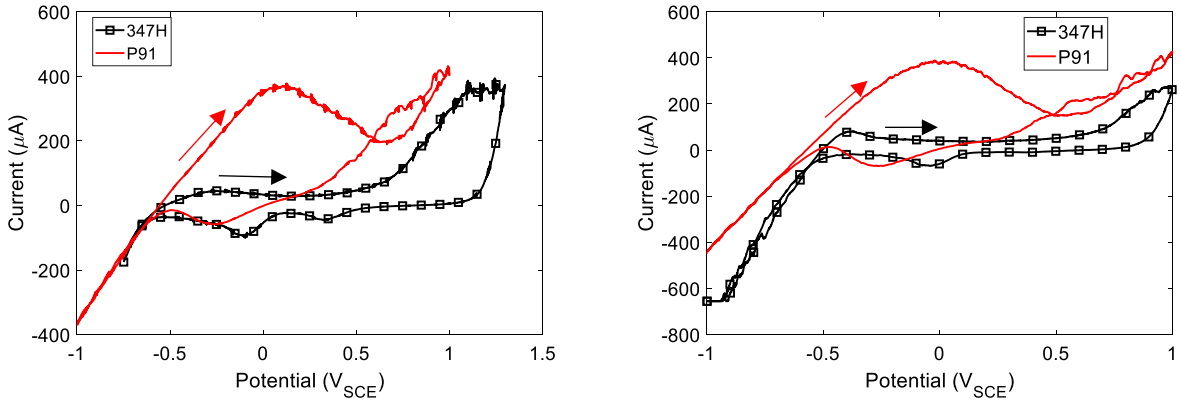

(a) 25°C (b) 50°C

Figure 11. Cyclic voltammetry scan

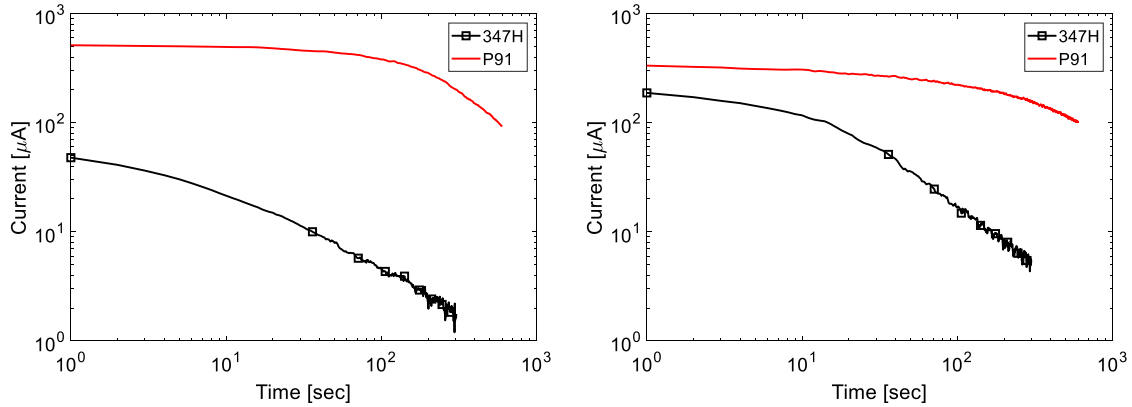

(a) 25°C (b) 50°C

Figure 12. Potentiostatic polarization scan

Corrosion rate calculations. All corrosion rates were calculated from equations 1 through 6 (6 to 8). As demonstrated from the corrosion rates of potentiodynamic scan and polarization resistance, both alloys have higher corrosion rate at higher temperature; furthermore, P91 has higher corrosion rate than 347H. The discrepancy of corrosion rate results between potentiodynamic scan and linear polarization is due to the large difference of scan rates. Potentiodynamic scan has a 5 mV/s scan rate, while linear polarization resistance has a 0.125 mV/s scan rate.

$$\eta_c = -\frac{2.3RT}{\alpha nF} log \frac{i_c}{i_0}, \beta_c = -\frac{2.3RT}{\alpha nF} \quad [1]$$

$$\eta_a = \frac{2.3RT}{\alpha nF} log \frac{i_c}{i_0}, \ \beta_a = \frac{2.3RT}{\alpha nF} \quad [2]$$

$$i_a = i_c = i_{corr} \quad [3]$$

$$Corrosion\ Rate = K_1 \frac{i_{corr}}{\rho} EW \quad [4]$$

$$Stern\ Geary\ Equation: i_{corr} = \frac{B}{R_p} \quad [5]$$

$$Stearn\ Geary\ Constant: B = \frac{\beta_a \beta_C}{2.303(\beta_a + \beta_c)} \quad [6]$$

TABLE IV. Corrosion rates

Alloy and Temperature	**Potentiodynamic Polarization, Scan Rate 5 mV/s**		**Polarization Resistance, Scan Rate 0.125 mV/s**		
	Corrosion Current Density [μA/cm^2]	Corrosion Rate [mm/year]*	Rp [Ω/cm^2]	Corrosion Rate [mm/year]*	Corrosion rate [mm/year]**
347H at 25°C	2.73	2.83×10^{-2}	2.47×10^{4}	2.74×10^{-2}	1.04×10^{-2}
347H at 50°C	5.81	6.03×10^{-2}	2.01×10^{4}	3.52×10^{-2}	1.44×10^{-2}
P91 at 25°C	4.71	5.26×10^{-2}	8.43×10^{2}	6×10^{-1}	1.70×10^{-1}
P91 at 50°C	9.94	11.1×10^{-2}	4.75×10^{2}	7.2×10^{-1}	3.27×10^{-1}

*Corrosion rate determined from Tafel slopes
**Corrosion rate determined from Stearn Geary Equation

Conclusions

Multiple conclusions can be made from the autoclave and electrochemical experiments.

- The electrochemical experiments show that corrosion rate for each candidate alloy increases as temperature increases, which is in good agreement with kinetic predications.
- Both the autoclave and electrochemical test results prove that 347H has better corrosion resistance than P91. 347H has less mass change than P91 in all autoclave exposure tests. The electrochemical corrosion rate calculations demonstrate that 347H has lower corrosion rate than P91
- Based on the cyclic voltammetry results, P91 is susceptible to localized corrosion.
- As demonstrated from the composition of conditions 2 and 3, corrosion mostly happens when water is present in liquid form. Thus, this conclusion can be extrapolated to sCO2 cycles: aqueous corrosion mostly happens during the shutdown period when water condenses.

Acknowledgments

This work was performed in support of the U.S. Department of Energy's Fossil Energy (FE) Crosscutting Technology Research Program. This research was supported in part by appointments (RR and LT) to the National Energy Technology Laboratory Research Participation Program sponsored by the U.S. Department of Energy and administered by the Oak Ridge Institute for Science and Education. The authors would like to thank the following people for their hard work and contribution to this project: Mr. Jeffrey Oberfoell, Dr. Randal Thomas, Dr. Richard Oleksak, Dr. Nicolas Huerta, Dr. John Baltrus, Dr. Alvaro Rodriguez, and Dr. Monica Kapoor, all with NETL. Discussions with 8 Rivers Capital personnel about direct supercritical CO_2 power cycles are appreciated.

References

1. X. Lu, *IEA Clean Coal Centre,* "Novel sCO2Allam Cycle for High-Efficiency, Low Cost and Emission-free Power Generation," (2016)
2. M. Kapoor, Private Communication, (2017)
3. L. Teeter, *M.S. Thesis, Materials Science Program, Oregon State Univ*., "Corrosion of Carbon and Stainless Steels in H_2O-sCO_2 Environments for Power Cycle Applications," Corvallis, OR (2016).
4. L. Teeter et al., *ECS Trans.*, "Corrosion Behavior of Austenitic Stainless Steel in Supercritical CO_2 containing O_2 and H_2O," Albany, OR (2016)
5. S. Sim et al., *Corrosion Vol. 68, No. 4.* "Use of Aqueous Solutions to simulate Supercritical CO_2 Corrosion," Clayton, Australia (2011)
6. M. Fontana, *McGraw-Hill, Inc*. Corrosion Engineering, (1986)
7. D. A. Jones, *Prentice-Hall. Inc.* Principles and Prevention of Corrosion, Upper Saddle River, NJ (1996)
8. ASTM G102-89(2015)e1 Standard Practice for Calculation of Corrosion Rates and Related Information from Electrochemical Measurements, ASTM International, West Conshohocken, PA (2015)